Inorganic Chemistry Communications 138 (2022) 109308

Contents lists available at ScienceDirect

Inorganic Chemistry Communications

journal homepage: www.elsevier.com/locate/inoche

Short communication

Elaboration, characterization and applications of SnO_2, 2 %Gd-SnO_2 and 2 %Gd-9 %F-SnO_2 thin films for the photocatalytic degradation of MB by USP method

Sabrina Roguai *, Abdelkader Djelloul

LASPI²A Laboratoire des Structures, Propriétés et Interactions Inter Atomiques, Université Abbes Laghrour, Khenchela 40000, Algeria
Department of Science of matter, Abbes Laghrour University, Khenchela, Algeria

ARTICLE INFO

Keywords:
SnO_2
2%Gd-SnO_2
and 2%Gd-9%F-SnO_2 films
X-ray diffraction
SEM
EDAX
FTIR
and Optical properties
Electrical properties
Photocatalytic

ABSTRACT

In this study, SnO_2, 2 %Gd-SnO_2, and 2 %Gd-9 %F-SnO_2 films were grown from tin chloride solutions by the ultrasonic spray technique on ordinary microscope glass substrates heated to a fixed temperature of 450 °C for photocatalytic application. The microstructural characterization of the thin films obtained was performed using X-ray diffraction (XRD), SEM, EDAX, and Infrared Spectroscopy (IR). The optical properties of thin films were studied by UV–Visible spectroscopy. To examine the electrical properties, we use the four-point method, the Seebeck effect and the Mott Shottky analysis. X-ray difraction reveals the formation of the routile phase of SnO_2 in all thin films with average crystallite size estimated in the range of 24–62 nm. The co-doping in (Gd-F) permitted an improvement of the thermoelectric properties of SnO_2. Moreover, we have demonstrated that an increase in grain size allows toimprove the Seebeck coefficient, to increase the electrical conductivity, on the other hand the doping in (Gd), presents a decrease in the size of the crystallites, which improves the degradation of methyl blue. The UV–Visible spectra of optical transmission of the layers show that the pure, doped and co-doped SnO2 films are of good quality with a transmittance of 73–83% in the visible and have an optical gap evaluated between 3.89, 3.98 and 3.99 eV respectively.

1. Introduction

The tin oxide is an n-type semiconductor with a broad bandwidth ranging from 2.7 to 4.6 eV, with a full valence band derived from the O 2p level (O^{2-} :1s^2 2 s^2 2p^6 3 s^0) and an empty conduction band from the Sn 5 s level [1]. The electronic configuration of tin (Sn: 1 s2 2 s2 2p6 3 s^2 3p^6 4 s2 3d^{10} 4p^6 4d^{10} 5 s^2 5p^2) provides for two sets of organic combinations corresponding to valences 4 and 2, tin finds the much more stable valence 4. The p states of oxygen represent a band at bond energies between 0 and 2 eV, this constitutes an energy band of 2 to 5 eV between the Sn 5p and O 2p orbitals. The lowest part of the valence band would result from strong interactions between the Sn 5 s and O 2p states. The last core levels of Sn 4d tin (the Sn 4d5/2 and Sn 4d3/2 states) are located at 22.2 and 23.2 eV respectively. The valence band is characterized by a high binding energy with hybridization of O 2p-Sn 5 s and O 2p-Sn 5p [1]. Regarding the conduction band, the lowest empty energy level is Sn 5 s, followed by Sn 5p states [1]. The interest of compounds with a band gap energy higher than 3.6 eV lies in the transparency in visible light of these compounds. On the other hand, this band gap energy is large enough not to allow carrier activation at high temperature, a process that strongly decreases the Seebeck coefficient. SnO_2 presents a single stable phase at atmospheric pressure, known as cassiterite and adopts a quadratic rutile type lattice.

Tin oxide crystallizes with a rutile-type tetragonal structure [2-4]. Its lattice (a = b = 4.737 Å and c = 3.185 Å) contains six atoms [5]: two tin atoms (RSn^{4+}= 0.71 Å) and four oxygen atoms (RO^{2-}=1.40 Å). Each tin atom is the center of an almost regular octahedron formed by six oxygen atoms, while each oxygen atom is surrounded by three tin atoms located at the vertices of an isosceles triangle. The description of the crystallographic orientation of the lattice varies according to the method of elaboration of the tin oxide [6]. Oxygen vacancies in thin films are the predominant type of defect, and interstitial tin atoms can easily diffuse to the surface and be oxidized there. COX et al [7] classify these vacancies into bulk and surface vacancies. Oxygen vacancies in the tin oxide layers result in an n-type semiconductor [6]. The concentration of electrons in pure SnO_2 results primarily from a lack of stoichiometry [8],

* Corresponding author.
E-mail address: rog.sabrina@yahoo.fr (S. Roguai).

https://doi.org/10.1016/j.inoche.2022.109308
Received 6 December 2021; Received in revised form 10 February 2022; Accepted 13 February 2022
Available online 17 February 2022

which creates additional donor-like electronic states within the band gap. Indeed, the oxygen gap thus created has two electrons that can bind to Sn^{4+} tin atoms, they then become Sn^{2+} and behave as electron donors. This means that the conductivity of SnO_2 depends on the existence of donor states near the conduction band formed by the oxygen vacancy [9]. When SnO_2 is perfectly stoichiometric, it behaves like an insulator at room temperature [8]. Its resistivity is probably on the order of 10^6 Ωm [10], the latter generally varies between 10^{-4} and 10^6 (Ωm) [9].

The physical and chemical characteristics of tin oxide can be modified by doping. Doping at low mass percentage allows to increase considerably the conductivity of a semiconductor, and thus to limit its ohmic loss. Tin oxide can be doped with F [11], Sb [12], Cu, Ni [13], In [14], Gd [15] and with the noble metals Pd and Pt [6]. The use of dopants such as Gd, In, F, and Sb has been frequently employed to obtain transparent thin films on glass substrates. These dopants are defects in the tin oxide films [6,15]. This means that the dopant can change the orbital electronic distribution of Sn. A charge from the dopant distorts the geometrical structure of the molecules [16] and generates the localized levels in the gap. The dopants change the position of the fermi level [6], for example, it is near the conduction band in the case of doping with Sb or F (donor), in the case of doping with In or Pd (acceptor) the fermi level is near the valence band. The Pt doping has no influence on the fermi level.

Thin films of SnO2 doped with rare earth metals (lanthanides + scandium + yttrium) have attracted a lot of attention because of their numerous applications. Among these rare earths gadolinium, the doping of Gd-SnO_2 have applications in the field of sensors, photocatalysts, medicine, metallurgy, in glasses and ceramics and also in some lamps (fluorescent, …) etc. [17,18]. It is also used in magnets. Very little gadolinium is found in nature, because it is present in small quantities. Other studies show that the doping of tin oxide with gadolinium enhances the degradation of pollutants by varying the concentration of oxygen vacancies in the SnO_2 crystal lattice [19].

Fluorine-doped SnO_2 (FTO) is a transparent conductive oxide that exhibits a good figure of merit, high optical transparency in the visible combined with high electrical conductivity, in addition to its chemical and thermal stability make them a TCO substitute for ITO [20]. Manikandan et al. Were interested in studying the effect of fluoride ion doping of SnO_2 thin films on the photocatalytic activity for MB (methylene blue) dye degradation. The FTO films show a photocatalytic activity of 95% while that of undoped SnO_2 is 87%, the authors interpreted this evolution by the generation of a large number of electrons by the fluoride ions incorporated in the SnO_2 lattice which increases the production of reactive oxygen species responsible for the photo catalytic degradation of the dye [21]. The publications concerning the FTO are very rich and treat different subjects, namely, the elaboration by several techniques such as spray pyrolysis, RF magnetron sputtering and its applications [22].

Various physical and chemical synthesis methods have been developed to allow the obtaining of thin films and nanostructures of tin oxide, as examples we cite physical vapor deposition (PVD), chemical vapor deposition (CVD), sol gel and electrodeposition [23,24], pulsed laser deposition [25], RF sputtering [26] and sputtering pyrolysis [27].

In the present study, we have realized thin films of SnO_2, 2 %Gd-SnO_2 and 2 %Gd-9 %F-SnO_2 by the ultrasonic spray pyrolysis technique which presents several advantages, such as the simplicity of equipment, the low cost, the deposition on large and complex surfaces as well as the possibility to control the properties by adjusting the different deposition parameters. The main objective of this work is to study the influence of doping and co-doping on the different structural, microstructural, optical and electrical properties. Thus to study their performance in the degradation of methyl blue.

2. Experimental part

2.1. Film preparation

The spraying pyrolysis technique may be utilized to prepare SnO_2, $Sn_{0.98}Gd_{0.02}O_2$, and $Sn_{0.89}Gd_{0.02}F_{0.09}O_2$ thin films utilizing tin (IV) chloride pentahydrate [$SnCl_4{\cdot}5H_2O$], gadolinium trichloride [$GdCl_3$] (0.02 M, 0.05 g), and (HF) (0.09 M, 36 μl) as precursors of the host and dopant, respectively. At first, (0.18 M, 0.6 g) precursor host was dissolved in 1 ml hydrochloric acid in order to increase the solubility of the solution [28], stirring and heating at 80 °C in beaker, then were added 10 ml absolute ethanol, and 7 ml deionized water to obtain a solution that was stirred without heating for 30 min. Finally the deposition of SnO_2 will be performed on ordinary microscope glass substrates (30 × 10 × 1.2 mm^3) heated at a fixed temperature of 450 °C for 30 min with a solution flow rate of 0.25 ml/min. These substrates are cleaned in an ultrasonic bath in ethanol, then in acetone, then in distilled water; each step lasts ten minutes. Afterwards, they are heated in ambient air. The same procedure was also used to prepare 2 %Gd-SnO_2, and 2 %Gd-9 %F-SnO_2 thin films.

2.2. Analysis of the semiconductor–electrolyte interface

Mott-Schottky analyses were carried out in a 0.5 M Na_2SO_4 electrolyte under a frequency of 1 KHz at an applied voltage ranging from −1 to 0.2 V with an amplitude of 10 mV at each voltage. using the electrochemical device consisting of a three-electrode borosilicate glass cell, using a Pt counter electrode and a Hg/HgCl (SCE) reference electrode, and the potentials reported hereafter are for this reference electrode. The SC thin film of 4.75 cm^2. This analysis allows us to identify the type of conductivity of the SnO_2 thin films and to access the flat strip potential.

2.3. Photodegradation of MB

In this experiment, we use SnO_2, 2 %Gd-SnO_2, 2 %Gd-F-SnO_2 thin films to degrade Methylene Blue present in a solution of pH = 9 with a concentration [MB] = $8x10^{-2}$M. We use a photochemical reactor composed of a dark chamber to protect from UV radiations, a magnetic stirrer, allowing thanks to a magnetic bar the permanent homogenization of the solution to be treated and a beaker of 10 ml which is used to contain the solution to be treated. The thin layer is immersed in the MB solution (10 ml) in order to subject the surface deposit to the fuorescence light of a Philips germicidal lamp (G15T8/15 W) emitting at a wavelength of 254 nm. The distance between the lamp and the beaker has been fixed at 7 cm. A sample of the solution to be treated is taken at each time interval (30 min), and its absorbance is deduced by UV–Visible analysis

2.4. Characterization techniques

The prepared samples have been analyzed by X-ray diffraction (XRD) studies for structural characteristic, crystallographic orientation and average grain size determination employing an X-ray difractometer (MiniFlex600) with Cu Kα radiation, 0.15418 nm). For the surface morphology study, we used a scanning electron microscope (SEM) (TESCAN_VEGA3) equipped with energy dispersive X-ray spectroscopy (EDAX) for chemical analysis. The Fourier transform infrared spectroscopy (FTIR) was recorded in the 4000–400 cm^{-1} region, and the SpectroScan 80D UV–Vis spectrophotometer in the 190–1100 nm spectral range for transmittance determination. And for electrical properties (conductivity, resistivity…) we have used the four-point technique, and Seebeck coefficient has been set based on the detected Seebeck voltage and temperature difference from 0 K to 200 K with an interval of 20 K. Mott-Schottky was determined by a CHI660E electrochemical workstation (CHI Instruments, Shanghai Chenhua Inc).

3. Results and discussion

3.1. Structural characteristics

To investigate the crystallinity, we present the diffractogram of SnO_2, 2% Gd-SnO_2, and 2 %Gd-F-SnO_2 thin films in Fig. 1. From Fig. 1 displays peaks located at 2θ = 26.61°, 33.92°, 38.06°, ,51.68°, 54.61°, 61.98°, and 65.88°corresponding to the crystal planes of the (110), (101), (200), (211), (220), (310), and (301) rutile phases of SnO_2 respectively. The positions of the peaks obtained are in good agreement with the tetragonal rutile structure of SnO2 (JPDS 41–1445) [29]. Moreover, no supplementary Gd or F phases, or other phases were detected. This indicates a good substitution of Gd and F atoms into the SnO_2 structure, in the limits of XRD detection.

According to the data of the standard JCPDS the mesh parameters of SnO2 are a = b = 4.737 Å and c = 3.185 Å according to [29], The mesh parameters calculated in this study (a = b and c), of the undoped SnO2 thin films are equal to (a = b = 4.736 Å and c = 3.183 Å), as it shows them the Table.1 It can be seen that these are slightly lower than those given by the JCPDS, but they increase as a function of Gd doping and co-doping (F-Gd).

For the doped thin films (Gd), the intensity of the peaks is significantly decreased, with a shift of the peaks to smaller angles than the pure SnO_2 thin films. This can be interpreted by the difference in the ionic radii of Gd^{3+} ions (1.07 Å), which is greater than that of Sn^{4+} ions (0.69 Å), which confirms the substitution of Gd ions in the lattice of the tin oxide [30]. For (F-Gd-SnO_2) co-doped thin films, the increased intensity of the peaks is well determined and particularly the intensity of the (211) plane that can be due to the compensation of F in the existing oxygen vacancies that can improve the periodicity and therefore the crystal quality [31]. In addition, the shift observed in the doped layers is corrected in the co-doping case confirming the insertion of F in the SnO_2. The doping with Fluorine has little effect on the crystallization of tin oxide which is a result in agreement with those of Agashe et al [32]. Indeed, the diagrams of undoped and fluorine-doped SnO_2 show the same appearance. Similar results were also found for SnO_2:F deposited by Spray [33].

The characteristics of the lattice (a and c) are determined by the following formula [34], and are listed in Table 1.

$$\frac{1}{d_{hkl}^2} = \frac{(h^2 + k^2)}{a^2} + \frac{l^2}{c^2} \tag{1}$$

In which d is the interplanar distance and (*hkl*) is the Miller indices. The obtained values of the lattice parameters 'a' and 'c' and the c/a ratio of SnO_2, 2 %Gd-SnO_2 and 2 %Gd-9 %F-SnO_2 thin films are presented in Table 1. This values of the lattice parameters a and c are increasing. We can explain this increment by the larger ionic radii of Gd^{3+} ions (1.07 Å) versus Sn^{4+} ions (0.69 Å). Therefore, the c/a ratio rises, indicating an expanded lattice along the c-axis.

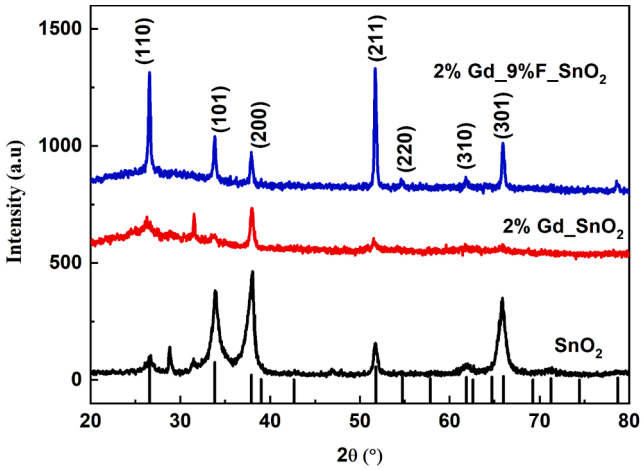

Fig. 1. XRD patterns of SnO_2, 2 %Gd-SnO_2 and 2 %Gd-9 %F-SnO_2 thin films.

The diffraction spectrum of X-rays has been used to determine the grain size D. The latter is calculated by applying the Debye-Scherrer formula [29], these values are tabulated in Table 1.

$$D = \frac{0.9\lambda}{\beta\cos(\theta)} \tag{2}$$

Where, D is the grain size, is the wavelength of the incident X-ray beam, =FWHM (full width at half maximum) is the width at half maximum of the diffraction line θ is the position of the diffraction peak considered. The distances are expressed in [Å] and the angles in radian. The crystallite size of 2 %Gd-SnO_2 thin films is decreased from 27 nm for the undoped films to 24 nm for the Gd-doped films. This reduction is due to the significant difference in the ionic radii of Gd^{3+} and Sn^{4+} that impacts the growth rate and diminishes the nucleation [30]. Thus the valence states of Gd^{3+} is less than that of the host Sn^{4+} cations. The low crystallite size leads to a greater surface/volume ratio, improving photocatalytic and gas sensing properties. In the case of 2 %Gd-9 %F-SnO_2 thin films the crystallites size is increased by a value greater than pure SnO_2 of 62 nm, this rise confirms the substitution by Gd^{3+} [35], and in addition this increase is due to the great atomic radiance of F that substituted the O atoms in the SnO_2 lattice [36]. Causing a rise in the number of nucleations that combine to form larger grains. [37]. As a result, the crystalline quality is enhanced and it is evident in the XRD results.

The distortion of the crystal can be calculated using the formula [38]:

$$\varepsilon = \frac{\beta}{4\tan(\theta)} \tag{3}$$

Calculated microstrain (ε) in Table1, was found to increase with Gd doping, this is due to the decrease of the particle size. However, the microstrain values for 2 %Gd-9 %F-SnO_2 thin films decreases due to increasing particle size.

3.2. Scanning electron microscopy

Fig. 2 shows the SEM micrograph of (a) SnO_2, (b) 2 %Gd-SnO_2 and (c) 2 %Gd-9 %F-SnO_2 thin films. It appears that the film is consistent and rough, without cracks. It can be seen that the sample is composed of various grain shapes with dark regions between the grains. In addition, the large faceted grains shown in this film indicate that coalescence growth is the cause of the crystallite formation.

3.3. EDAX studies

In order to determine the composition of the films, energy dispersive X-ray spectroscopy (EDAX) has been used. Fig. 3, shows the EDAX spectra of SnO_2 (a), 2 %Gd-SnO_2 (b), 2 %Gd-9 %F-SnO_2 (c) film prepared at 30 min. From Fig. 3, the same elements of our precursor Sn, O, Gd and F are present in the film. The other elements such as Si present in the spectrum are from our glass substrate [39]. This confirms the purity of the thin films. Composition of the SnO_2, 2 %Gd-SnO_2 and 9 %F-2 % Gd-SnO_2 thin films are listed in Table 2

3.4. FTIR analysis

FTIR spectroscopy is a structural analysis method that reveals the nature of the bonds between atoms in a molecule. In Fig. 4, present the FTIR spectra of the sample of SnO_2, 2 %Gd-SnO_2, and 2 %Gd-9 %F-SnO_2 in the range 4000–400 Cm^{-1}. All the spectra are quite similar and we notice that the absorption bands present the same bands with a different intensity. In general five IR absorption zones can be identified in the FTIR spectra of our samples. A broad absorption band located between 525 and 627 cm^{-1} which can be attributed to Sn-O vibrations and to the

Table 1
Structural parameters of SnO_2, 2 %Gd-SnO_2 and 9 %F-2 %Gd-SnO_2 thin films.

Sample	Plan (hkl)	$2\theta_{hkl}$ (deg.)	$d_{spacing}$ (Å)	B (deg.)	Lattice Constants (Å)			D (nm)	ε (%)
					a	c	c/a		
SnO_2	(1 1 0)	26.61	3.349	3.542	4.7364	3.1830	0.6720	27.62	
	(1 0 1)	33.92	2.642	3.542					0.443
	(2 0 0)	38.06	2.364	2.952					
	(2 1 1)	51.68	2.768	4.133					
2 %Gd-SnO_2	(1 1 0)	26.30	3.387	7.085	4.7899	3.1881	0.6655	24.11	
	(1 0 1)	33.76	2.654	7.085					0.705
	(2 0 0)	37.97	2.369	2.362					
	(2 1 1)	51.56	1.772	3.542					
2 %Gd-9 %F-SnO_2	(1 1 0)	26.56	3.355	1.771	4.7446		0.6748		
	(1 0 1)	33.88	2.645	1.476		3.2017		62.24	0.213
	(2 0 0)	37.96	2.370	2.066					
	(2 1 1)	51.69	1.768	1.476					

O-Sn-O bridge bond or to the antisymmetric vibrations of the M−O−M bonds (here: Sn-O-Sn), and this in very good agreement with the literature [40,41]. We do not observe any peak around 460/415/ and/or 560 cm^{-1} which represent typical Gd-O stretching of the cubic phase of Gd_2O_3 or the tetrahedral phase of GdO_2 [42]. The peak located around 1419 cm^{-1} can be attributed to the vibrations of the organic C-H residues [43]. The peak at 948 cm^{-1} represents the deformation of C = O or C-C [43]. The broad peak centered around 3445 cm^{-1} and the peak at about 1637 cm^{-1} is attributed to the vibrations of hydroxyl groups (O-H) of water adsorbed on the surface of the material [44]. It is evident that the intensity of the characteristic bands of the O-Sn and Sn-O-Sn bonds is greatly reduced with doping and co-doping, with a band shift in the case of 2 %Gd-F-SnO_2. The decrease in intensity and shift of the bands confirms the incorporation of Gd and F in the SnO_2 lattice.

3.5. Optical properties

The transmittance spectra for SnO_2, 2 %Gd-SnO_2 and 2 %Gd-9 %F-SnO_2 thin films are recorded at room temperature in Fig. 5 in order to examine their optical properties. Variation properties of the The dispersion parameters of the thin films were determined by a single-effect oscillator fit, suggested by Wemple and DiDomenico [45]. Full curves in Fig. 5 refer to the curve fit and the symbols depict the experimental data. The fgure indicates that the fit is reasonably good to the experimental data, and the values of d, Eg, n at 598 nm, and n∞ extracted by the fit [45] from experimental data are listed in Table 3.

It is observed that the average transparency in the visible range is between 73 and 83% in the visible which is strongly influenced by the doping and co-doping involving an increment of the transmittance. All the layers show significant oscillations in the visible range, which are related to the phenomenon of interference and are generated by the thickness of the layers. The interference bangs observed in the spectra are due to the multiple reflection of radiation between the two interfaces of the SnO_2 thin film (see Fig. 5), which clearly explains the homogeneity of our layers and that its surfaces are smooth and uniform [46]. A strong absorbance appears in the wavelength region below 380 nm due to the fundamental absorbance of the material (valence band - conduction band). We observe that the transmitance decreases with the increase of the thickness of the layers. While the doping improves the transmitance of the layers. We also note that the 2 %Gd-F-SnO_2 layer has the highest transparency in the visible.

The Fig. 5 displays an absorption edge in the near UV with a shift of this edge towards short wavelengths, showing that the addition of dopant (Gd, and Gd-F) tends to increase the gap of tin oxide following the Burstein-Moss effect (see Table 3) [47]. The Burstein-Moss effect, based on which the increase in carrier concentration due to doping results in a shift of the Fermi level, approaching the conduction band, and blocking certain weak states at the tail of the conduction band, thus causing a widening of the band gap by a magnitude Eg. This broadening expresses the shift of the absorption tail towards low wavelengths (high energy). This bandgap energy widening is also responsible for the transmission enhancement in the UV region. It is clear that such an effect is positive in the case of solar cells using SnO_2 as a collector because it increases the absorption of photons and improves the photon yield.

Based on the single oscillator energy (E_0) and the static refractive index (n_∞) from the fitted transmittance spectra given in Table 3 [45]. While the values of the dispersion energy (E_d) are determined according to the following relationship [48].

$$n_\infty^2 - 1 = \frac{E_d}{E_0} \tag{4}$$

The values of E_0 obtained are increasing with the doping and co-doping SnO_2 films and it is known that this value is inversely correlated with the crystalline properties which affirms the degradation of these properties in our case. The values of E_d (see Table 3) is decreased with the doping and co-doping SnO_2 thin films, confirming the substitution of Gd^{3+} and F^- ions in the SnO_2 lattice

The Fig. 6 gives the calculated values of the refractive index [49]. The values of the refractive index n of the obtained layers are decreased with the doping and co-doping to that of SnO_2, we note that the refractive index of the layers is affected by the presence of structural defects, that confirms the insertion of Gd^{3+} and F^- in the SnO_2 lattice [21]. This means that the decrease in refractive index is due to the change in density of the layers during processing. This will cause an increase in porosity as shown in Table 3. With this increase in porosity, a decrease in electrical resistivity is expected due to the strong bonding of crystallites.

The porosity P is calculated from optical constants using the Lorentz–Lorenz equation [50]:

$$P = 1 - \left[\left(n_{film}^2 - 1\right)\left(n_{bulk}^2 + 2\right)/\left(n_{film}^2 + 2\right)\left(n_{bulk}^2 - 1\right)\right] \tag{5}$$

Here the value of n_{flm} represents the refractive indices of porous SnO_2, 2 %Gd-SnO_2,2%Gd-9 %F-SnO_2 flms at 598 nm and nbulk represents the refractive indices of SnO_2 bulk which is 1.997 [51] at same wavelength, presented in Table 3, the values of the porosity is greater than that of pure SnO_2 synthesized under the same conditions at a value of P = 0.1047, which is explained by the change of the crystal structure. This increase leads to the increase of the surface d'adsorption [52].

3.6. Electrical properties

3.6.1. Measurement of resistivity

The electrical properties of tin dioxide layers depend strongly on

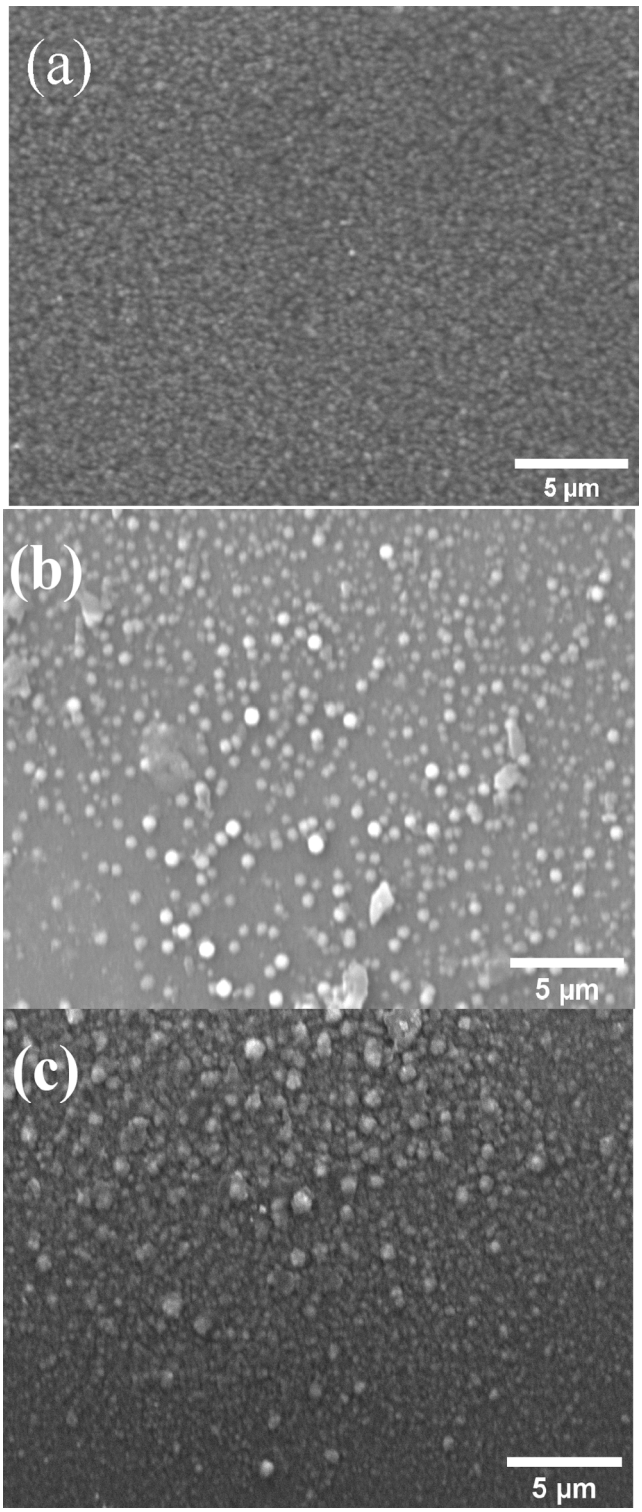

Fig. 2. Scanning electron microscope (SEM) images of (a) SnO_2, (b) 2 %Gd-SnO_2 (c) 2 %Gd-9 %F-SnO_2 thin films.

their composition (doping, stoichiometry) [53] and their structure (grain size, grain boundaries, porosity,…) [6,54]. Generally, the electrical conduction mechanism in SnO_2 films is controlled by the transport of charge carriers through the grain boundaries [54,55]. Grain boundaries [54,55]. An excellent transparent conducting oxide is defined by a high electrical conductivity combined with a high carrier concentration. The latter depends strongly on the mobility, when it was low, the carrier mobility was high, although the films were polycrystalline [13].

The measurement results of the surface resistance (square) made on our samples are reported in Table 4. The resistivity is deduced from the measured value of the surface resistance (square) knowing the thickness (d) of the films:

$$\rho = R_s \times d \tag{6}$$

It was found that the resistivity of 2 %Gd-SnO_2 doped films increases, this can be explained by the decrease in the carriers concentration lead to minimize the free electron density, indicating that Sn ions substituted by Gd ions, this explains the reduction in crystallite size [56]. To explain the very high resistivity of SnO_2 films, several hypotheses have been put forward. It is obvious that the electrical properties depend on the porous structure of the SnO_2 films and on the grain size, these properties are significantly affected by the conditions of elaboration and crystallization of the layers [57]. The discontinuity of the structure, thus created, prevents the transfer of electrons between the grains. The decrease of resistivity with the increase of the particle size could be explained by the reduction of the number of contact joints between the grains. We note that this decrease in resistivity is due to the increase of free charge carriers due to the increase of the quality of the films.

In the case of 2 %Gd-9 %F-SnO_2 thin films, the conductivity will be influenced by the chemical environment of the tin in the SnO_2 matrix. Thus, for low contents of fluorine introduced in the SnO_2 films deposited by spray method, fluorine will be able to substitute for oxygen with release of an electron to the conduction band. Moreover, the electrical resistivity values have been minimized, which may be attributed to the increase of the carrier concentration.The relationship between the electrical properties of tin oxide and nanostructure (porosity, grain size, thickness), stoichiometry and vacancy concentration, is of great complexity [58].

3.6.2. *Seebeck coefficient*

The measurement principle of the Seebeck coefficient is based on the presence of a voltage when a material is subjected to a temperature difference, based on the following relationship [59]:

$$S = -\frac{\Delta V}{\Delta T} \tag{7}$$

The evolution of the Seebeck coefficient at low temperature (0 K to 200 K) is shown in Fig. 7. All these samples have a negative Seebeck coefficient, this confirms that they are n-type semiconductors [60]. The value of Seebeck coefficient of 2 %Gd-SnO_2 sample is about 148 µV/K, this value is higher than that of SnO_2 (76 µV/K). The substitution of Gd^{3+} ions into the SnO_2 mesh leads to a change in the Seebeck coefficient of the samples. Thus, the Seebeck coefficient of the 2 %Gd-9 %F-SnO_2 sample (86 µV/K) is decreased almost twofold compared to that of the 2 %Gd-SnO2 sample. Because the Seebeck coefficient and the carrier concentration typically relate inversely [61], it is important to find the carrier concentration, Eq(8) [59], including the effective density in the conduction band, Eq (9)[62]

when, $|S| > 75$ µV/K

$$m_S^* = \frac{h^2}{2k_BT}\left\{\frac{3n}{16\sqrt{\pi}}\left(exp\left[\frac{|S|}{(k_B/e)} - 2\right] - 0.17\right)\right\}^{2/3} \tag{8}$$

$$N_C = 2\left(\frac{2\pi m_s^* k_B T}{h^2}\right)^{3/2} \tag{9}$$

In which e is the charge of the carrier, k_B is the Boltzmann constant, T is the absolute temperature, h is Plank's constant, and m_S*(m_S*= 0.216 m_0) is the effective Seebeck mass of SnO_2, and n is the carrier concentration. The values of charge concentration of our films are presented in Table 5, it can be noticed that pure, doped and co-doped SnO_2 thin films are in degenerated state ($n > N_C = 3.63x10^{18}$ cm^{-3}). The value of the carrier concentration n of SnO_2 is 1.9×10^{19} cm^{-3} that explains its conductivity.

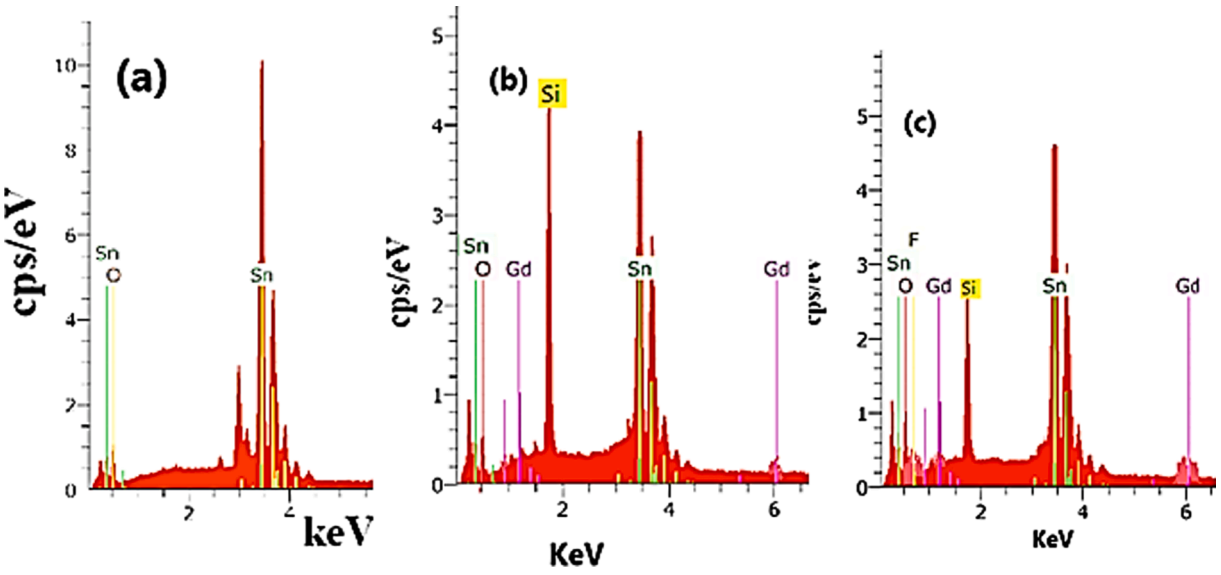

Fig. 3. EDAX elemental composition analysis of SnO_2 (a), 2 %Gd-SnO_2(b), 2 %Gd-9 %F- SnO_2 (c) thin films.

Table 2
Composition of the SnO_2, 2 %Gd-SnO_2 and 9 %F-2 %Gd-SnO_2 thin films obtained by statistical analysis of EDS spectra.

$Sn_{1-x}Gd_xF_yO_2$[x = 0, 2, y = 9] "Nominal'' x and y content (at.)	Sn (at. %)	O (at. %)	Gd (at. %)	F(at. %)
SnO_2	54.68	45.32	–	–
$Sn_{0.98}Gd_{0.02}O_2$	55.49	44.33	0.18	–
$Sn_{0.89}Gd_{0.02}F_{0.09}O_2$	51.08	40.09	0.18	8.65

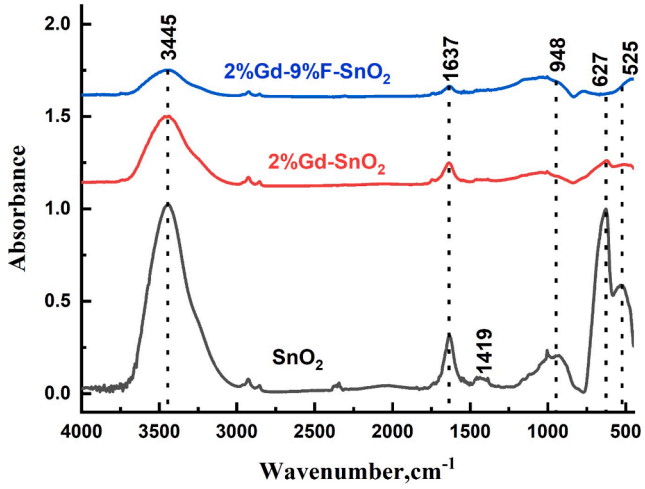

Fig. 4. FTIR spectra of SnO_2, 2 %Gd-SnO_2, and 2 %Gd-9 %F-SnO_2 films grown onto glass substrate by ultrasonic spray pyrolysis at 450 °C in the game 400–4000 cm^{-1}.

We notice that the 2 %Gd-SnO_2 thin films having the largest value of $|S|$, which interpreted by the minimum carrier concentration values is 5.3×10^{18} cm^{-3}., and on the other hand this low carrier concentration values is the closest to N_C which indicates that the 2 %Gd-SnO_2 films is less degenerate compared to the pure and co-doped SnO_2 films, these findings confirms the substitution of Gd^{3+} in the SnO_2 lattice. However, the small difference in $|S|$ and carrier cocentration values between the undoped and co-doped films confirmed the substitution of oxygen by fluorine, a fact that is verified by the close proximity of the degenerate state (see Fig. 8). The oxygen vacancies and interstitial cations are

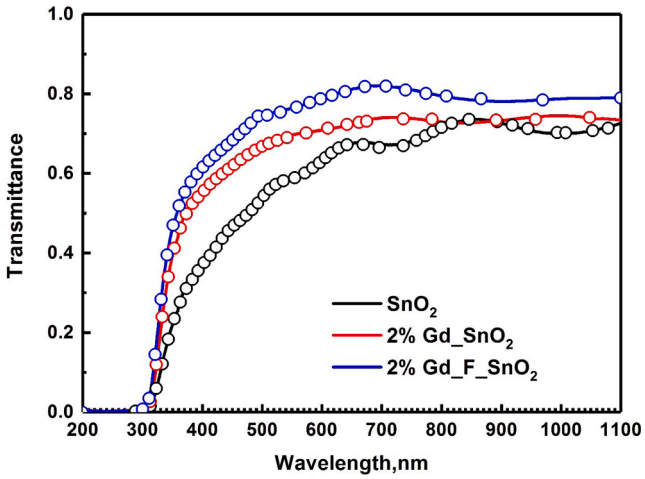

Fig. 5. Transmission spectra of SnO_2, 2 %Gd-SnO_2, and 2 %Gd-9 %F-SnO_2 thin flms deposited on glass substrate at 450 °C. Measured (circles) and calculated (solid lines) transmittance spectra of flms.

Table 3
Dispersion parameters of the SnO_2, 2 %Gd-SnO_2, and 2 %Gd-9 %F-SnO_2 films extracted by fitting the experimental data.

Samples	Thickness (nm)	Eg (eV)	n at 598 nm	n_∞	E_0	E_d	P
SnO_2	693	3.89	1.85	1.79	5.44	12.00	0.1047
2 %Gd-SnO_2	440	3.98	1.65	1.62	5.57	9. 05	0.2690
2 %Gd-9 %F-SnO_2	353	3.99	1.62	1.60	5.58	8. 71	0.2960

known to be the source of conductivity in non-stoichiometric intrinsic oxides, and oxygen vacancies are the predominant defects in tin oxide [24]. Therefore the increase of the carrier concentration with the co-doping (which corresponds to the values of $n = 5.3 \times 10^{18}$ cm^{-3} to $n = 1.5 \times 10^{19}$ cm^{-3} for 2 %Gd-SnO_2 and 2 %Gd-9 %F-SnO_2 thin films respectively) can be explained by the creation of oxygen vacancies with a release of of electrons in the SnO_2 lattice according to the reaction

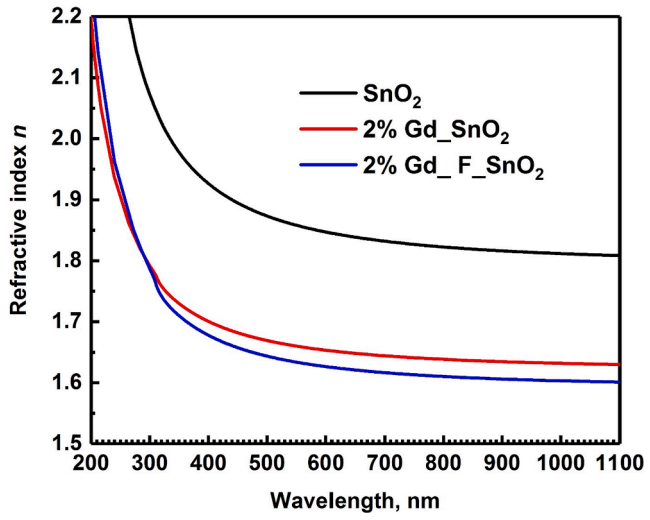

Fig. 6. Refractive index of SnO_2, 2 %Gd-SnO_2, and 2 %Gd-9 %F-SnO_2 films.

Table 4
Surface resistance, resistivity and electrical conductivity of SnO_2, 2 %Gd-SnO_2 and 2 %Gd-9 %F-SnO_2 thin films

Samples	Square resistance, Ω	resistivity ($\times 10^{-2}$), Ω cm	Conductivity, Ω^{-1} cm^{-1}
SnO_2	260	1.8	55
2 %Gd-SnO_2	670	2.9	10
2 %Gd-9 %F-SnO_2	380	1.3	74

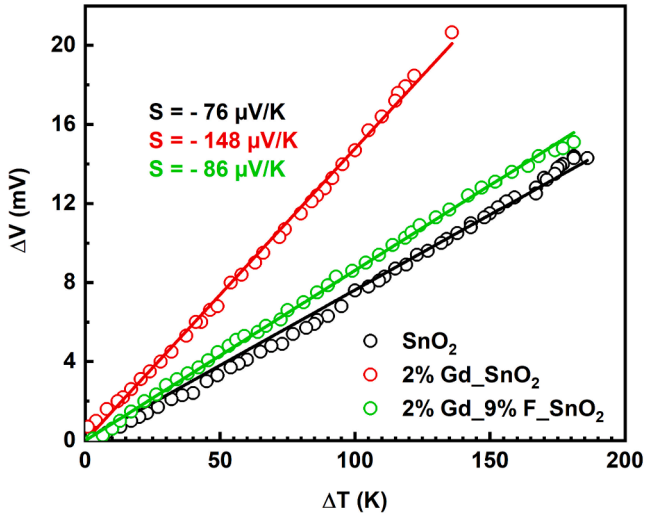

Fig. 7. Seebeck coefficients for SnO_2, 2 %Gd-SnO_2, and 2 %Gd-9 %F-SnO_2 thin films.

Table 5
Carrier concentrations (n), and Fermi energy (EF), of SnO_2, 2 %Gd-SnO_2, 2 %Gd-9 %F- SnO_2 sprayed thin films.

	n, cm^{-3}	E_F, meV
SnO_2	1.9×10^{19}	96
2 %Gd _SnO_2	5.3×10^{18}	49
2 %Gd _9%F_SnO_2	1.5×10^{19}	85

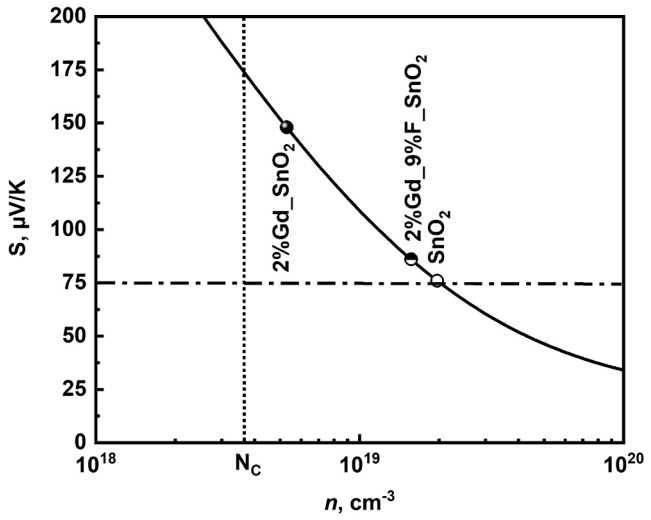

Fig. 8. Seebeck coefficients as a function of carrier concentrations for SnO_2, 2 %Gd-SnO_2, and 2 %Gd-9 %F-SnO_2 thin films.

(10), presented by the notation of KrÖger-Vink notation [63].

$$O_O^X \rightarrow V_{\ddot{O}} + 2e^- + \frac{1}{2}O_2 \tag{10}$$

Moreover, this degeneracy in our samples is verified by the evaluation of the Fermi energy level (E_F) according to this relation [64]:

$$E_F = \frac{\pi^2 k_B^2 T}{3|e||S|} \tag{11}$$

The Fermi energy values calculated are listed in Table 5, the value of Fermi energy for undoped SnO_2 (96 meV) is smaller then the valus calculaterted by first-principles calculations based on the density functional theory (427 meV) [65], that indicates that our thin film elaborated by the USP technique is conductive which confirms by the previous results of the carrier concentration. For the 2 %Gd-9 %F-SnO_2 films the values of Fermi energy are 49 and 85 meV respectively, the reduction of E_F with doping can be interpreted by the substitution of Sn^{4+} ions by Gd^{3+} ions. Subsequently, the E_F values are regained with co-doping as fluorine (donor), generates the localized levels in the gap and thus change the position of the fermi level near the conduction band [6]. This can be explained as follows: when fluorine is incorporated into the tin oxide layers, each F^- anion substitutes an O^{-2} anion in the lattice and the F^- substituted anion has more free electrons because it can play the role of the O^{-2} anion with an excess electron easily ejected into the conduction band ($O^{2-} + F \rightarrow O + F^- + e^-$), this results in an increase of free electrons responsible for the decrease of the resistivity value.

3.6.3. Mott-Schottky (MS) analysis

Mott-Schottky measurements are useful for determining the charge carrier density (N_D) and flat band potential (E_{fb}) and their variation with electrolyte pH. Fig. 9 shows the M–S curves of SnO_2, 2 %Gd-SnO_2 films obtained in electrolytes at PH = 9. These curves are obtained by plotting the variation of the differential capacitance of the space charge region as a function of the potential applied in a 0.5 M Na_2SO_4 electrolyte with a frequency of 1 kHz. by applying equation (12) [66].

$$\frac{1}{C^2} = \frac{2}{\varepsilon s \varepsilon_0 A^2 e N_D}\left(V - V_{fb} - \frac{K_B T}{e}\right) \tag{12}$$

In which C corresponds to the interfacial capacitance, εs denotes the dielectric constant of the semiconductor, ε_0 the free-space permittivity, e the electronic charge, N_D the donor density, V the applied potential, V_{fb} the flat-band potential, k_B the Boltzmann constant and T the absolute temperature. The linear part of the M–S curves has a positive slope; this

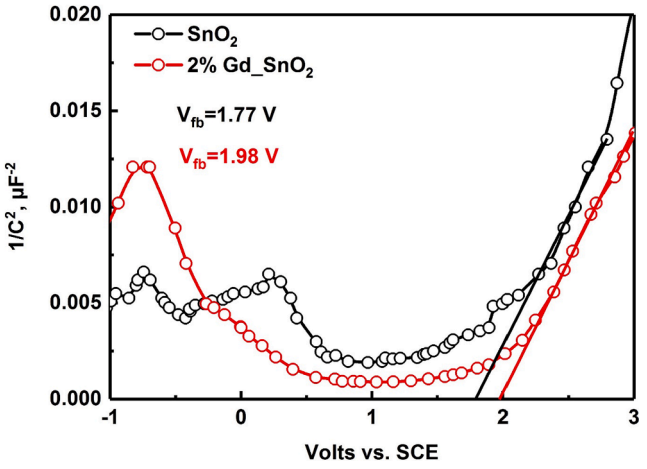

Fig. 9. Mott-Schottky curves of SnO_2, and 2 %Gd-SnO_2 thin films.

indicates n-type semiconductivity for all samples [67,68], from this slope the charge carrier density ND can be calculated ($Slope = \frac{2}{\varepsilon s \varepsilon_0 A^2 e N_D}$). Extrapolation of the linear part of the M−S curves to $\frac{1}{C_{CS}^2} = 0$ leads to the determination of the values of the flat band potentials. These parameters are determined experimentally and are grouped in Fig. 9. The flat band potential (E_{fb}) shifts to the most positive values with doping, explaining this shift of flat band potential to more positive values by the low crystallinity of these films and is consistent with XRD results

3.7. Photocatalytic activity

The sprayed 2 %Gd-SnO_2 and 2 %Gd-9 %F-SnO_2 thin films were tested to evaluate their photocatalytic activity in the degradation of MB dye under UV irradiation. Fig. 10 depicts the absorption of the MB solution due to photodegradation for various irradiation times. The decrease in UV–visible absorption spectra allowed us to follow the photodegradation of MB (with maximum intensity at $\lambda_{max} = 664$ nm) from MB. It is clear that the 2 %Gd-9 %F-SnO_2 thin films have a low photo-catalytic effect of the MB solution. However, the 2 %Gd-SnO_2 thin films reveal a higher reactivity with MB

Apparent degradation rate constant (k) was taken as a basic kinetic parameter in order to evaluate the photocatalysts, with first order kinetics being assigned. Fig. 11 displays the kinetics of the degradation process of methylene blue in solution, and the calculations of the kinetic parameters of this degradation are shown in Table 6, according to the following formula (13) [69].

$$A = X^*\exp(-k^*t) + E \quad (13)$$

While the speed constant (pseudo) of order k is the inverse of that of the time used (min^{-1}), X represents the amplitude of the process, E corresponds to the end point, both have the same units as the measured value A.

Apparent degradation rate constant (k) was taken as a basic kinetic parameter in order to evaluate the photocatalysts, with first order kinetics being assigned,

The rate constant k values for the thin films were 2 %Gd_SnO_2 (0.0084 min^{-1}), 2 %Gd_9%F_SnO_2 (0.0006 min^{-1}), an irregular variation of the kinetic constant with the concentrations of Gd and F is obtained [70].

The higher k-value of 2 %Gd_SnO_2 thin films has verified that the effect of Gd that increased the separating efficiency of photoinduced charge carriers, optical absorption in the visible region and their morphology is the reason for the increased photocatalytic performance.

The photocatalysis is based on the absorption, by a photocatalyst generally semi-conductor, of a light radiation of energy higher or equal to the energy (Eg) of its band gap. This energy absorption causes

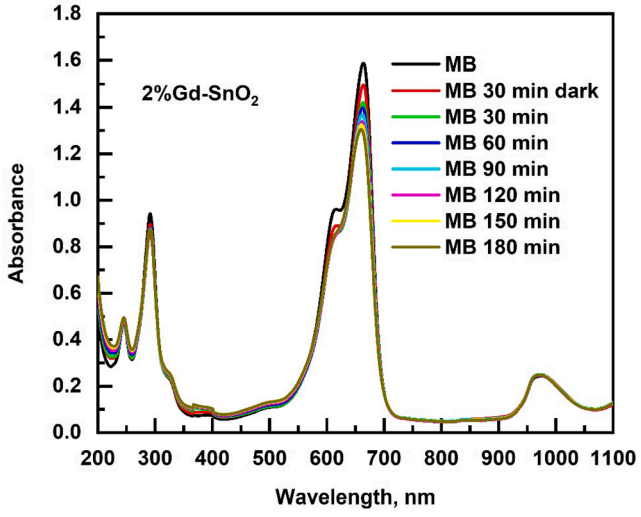

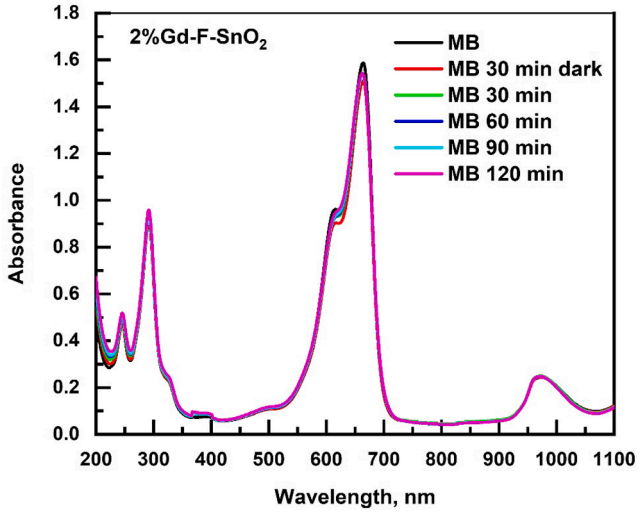

Fig. 10. The efect of 2 %Gd-SnO_2, and 2 %Gd-9 %F-SnO_2 thin flm on the absorption spectra of MB solution (10 ml, 8×10^{-2} M) for diferent reaction time under UV irradiation.

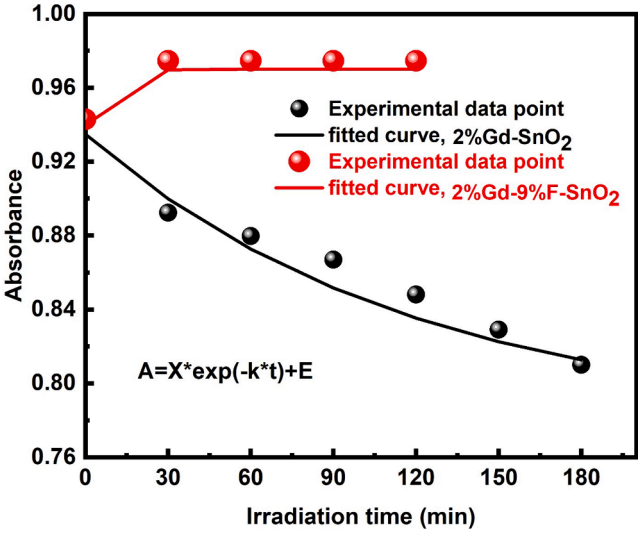

Fig. 11. Degradation kinetics of MB aqueous solutions by 2 %Gd-SnO_2, and 2 %Gd-9 %F- SnO_2 thin flms.

Table 6
Pseudo-first-order kinetic parameters of MB degradation.

Samples	Value			Standard deviation			R^2
	K(min^{-1})	X	E	K(min^{-1})	X	E	
2 %Gd-SnO_2	0.0084	0.1564	0.7784	0.0026	0.0235	0.0254	0.9800
2 %Gd-9 %F-SnO_2	0.0006	−0.0300	0.9700	0.0192	0.0001	9.2361	0.9998

electrons (*e* -) to pass from the valence band (VB) to the conduction band (CB) creating electron gaps, commonly called "holes" (h +) in the valence band.

The electron-hole pairs (e-/ h +) thus generated give the solid oxidizing-reducing properties. These pairs (e -/ h +) can recombine, either directly or indirectly (via surface defects) through radiative or non-radiative processes, without giving rise to a chemical reaction (charge recombination).

On the other hand, if the photogenerated charges migrate to the surface and encounter an electron acceptor (A) and an electron donor (D) adsorbed on the surface, a charge transfer occurs.

$$SC \rightarrow e^-_{CB} + h^+_{VB} \quad (14)$$

$$A_{ads} + e^- \rightarrow A^{\cdot -}_{ads} \quad (15)$$

$$D_{ads} + h^+ \rightarrow D^{\cdot +}_{ads} \quad (16)$$

Thermodynamically, when an irradiated semiconductor is in contact with surface adsorbed electron donors and acceptors, a redox reaction will be able to take place under given experimental conditions (temperature, solvent, pH, reactant concentration) at redox potentials between E_{CB} and E_{VB}. Oxidation reactions will occur at potentials below the valence band potential ($Eox < E_{vB}$), whereas reduction reactions will occur if $Er_{ed} > E_{CB}$.

The most direct pathway for the formation of the $HO^{\bullet}$ radical is the hole oxidation, h^+, of H_2O donors or hydroxyl ions (OH^-), adsorbed on the surface of the semiconductor:

$$H_2O + h^+ \rightarrow HO^{\cdot} + H^+ \quad (17)$$

$$OH^- + h^+ \rightarrow HO^{\cdot} \quad (18)$$

These different radicals can react with organic compounds to form CO_2 and H_2O (mineralization). However, many organic compounds (P) are susceptible to direct oxidation by photogenerated holes by forming the cation radical P^+:

$$P + h^+ \rightarrow P^{\cdot +} \quad (19)$$

The cation-radicals $P^{\bullet +}$ can then react with, for example, H_2O, O_2, and $O_2^{\bullet -}$, to lead to the final oxidation products. The overall mechanism of heterogeneous photocatalysis is thus broken down into five independent steps, (●Diffusional migration of reactants from the fluid phase to the catalyst surface. ●Adsorption of at least one reactant. ● Reaction at the surface.●Desorption of reaction products. ●Diffusional migration of reaction products from the catalyst surface to the fluid phase).

In addition, research reveals that several factors influence the photoactivities of photocatalysts, such as the crystallinity, grain size, specific surface area, surface morphology and surface condition (surface OH radicals), which are not independent but strongly related to each other [71,72].

The 2 %Gd-SnO_2 film has the smallest crystallite size (24 nm) and a narrower energy band gap (3.98 eV), compared to the 2 %Gd-9 %F-SnO_2 film with a larger crystallite size (62 nm), and a slightly larger energy band gap (3.99 nm). The co-doped films have low MB degradation capacity while the doped layers exhibit higher potency due to the spectral response in the visible light region. In this case, the photo-catalytic activity of the 2 %Gd-SnO_2 and 2 %Gd-9 %F-SnO_2 thin films can be explained by the fact that the oxygen vacancies are the most important defect type, and interstitial tin atoms can easily diffuse towards the surface and be oxidized there [24], that due to the decrease of recombination rate and activation energy improving the photocatalytic activity.

4. Conclusion

Thin films of SnO_2, 2 %Gd-SnO_2 and 2 %Gd-9% F-SnO_2 were deposited on glass substrates using spray pyrolysis method at 450 °C for 30 min. The effect of doping and co-doping on the structural, optical, electrical and photo-catalytic properties of these films has been studied. We characterized these doped, co-doped and undoped thin films by various methods, X-ray diffraction (XRD) for structural study, SEM, EDX and FTIR for morphology, composition and structural analysis of our films, UV–Visible spectroscopy for optical properties study, four point method, Seebeck and Mott shottky effect to determine the electrical properties of our films as well as methyl blue degradation tests under UV irradiation.

XRD analysis of the samples shows that all samples crystallize under the tetragonal structure with different preferential orientations, and the intensity of the peaks increases with co-doping. Grain sizes calculated from the Scherrer equation vary between 27.24 and 62 nm for the SnO_2, 2 %Gd-SnO_2 and 2 %Gd-9 %F-SnO_2 thin films respectively. The morphological study by SEM shows that we are in the presence of a uniform structure with a spherical morphology of the crystallites. The FTIR spectrum shows the presence of characteristic vibration peaks O-Sn and Sn-O-Sn of about 525 and 627 cm^{-1} for all the films obtained. The UV–visible spectroscopy shows that the transmittance of the films varies between 73 and 83% respectively. The values of the optical gap energy of our films is in increase with the doping and co-doping. Mott-Schottky and Seebeck coefficient measurements showed, n-type conductivity for all samples and optimum charge carrier concentration of 1.9×10^{19} cm^{-3}, 5.3×10^{18} cm^{-3} and 1.5×10^{19} cm^{-3} for the films obtained at SnO_2, 2 %Gd-SnO_2 and 2 %Gd-9 %F-SnO_2 respectively, regarding the conductivity values the co-doped thin films has the highest values of 74 Ω^{-1} cm^{-1}. Photocatalytic tests indicate the efficiency of 2 %Gd-SnO_2 films due to their morphology. This investigation reveals that the co-doped films possess interesting properties that can be proceeded for the photovoltaic application.

Declaration of Competing Interest

The authors declare the following financial interests/personal relationships which may be considered as potential competing interests: Roguai Sabrina reports financial support was provided by LASPI2A Laboratoire des Structures, Propriétés et Interactions Inter Atomiques, Université Abbes Laghrour, Khenchela 40000, Algérie. Roguai Sabrina reports a relationship with LASPI2A Laboratoire des Structures, Propriétés et Interactions Inter Atomiques, Université Abbes Laghrour, Khenchela 40000, Algérie that includes: employment.

Acknowledgement

Funding was provided by the General Direction of research and development technologies/ Ministry of Higher Education and Research Sciences DGRSDT/ MESRS, Algeria. The financial support from Abbes

Laghrour University of Khenchela (Algeria). The authors would like to thank the National Project Research (PNR) and LASPI2A Laboratory of Khenchela University (Algeria) for their financial support of this research project. The authors thank Pr. Abdecharif Boumaza for FTIR analysis, Laboratoire des Structures, Propriétés et Interactions Inter Atomiques (LASPI2A), Université Abbes Laghrour, 40000 Khenchela, Algeria.

Author contributions

The manuscript was written through contributions of all authors. All authors have given approval to the final version of the manuscript.

References

[1] M. Batzill, K. Katsiev, J.M. Burst, U. Diebold, A.M. Chaka, B. Delley, Phys. Rev. B72 (165414) (2005) 1–20.
[2] K.H. Kim, J.S. Chun, Thin Solid Films 141 (1986) 287–295.
[3] D. Wang, S.h. Wen, J. Chen, S. Zhang, F. Li, Physical review B 49 (1994) 14282–14285.
[4] R. Rai, T.D. Senguttuvan, S.T. Lakshmikumar, Comput. Mater. Sci. 37 (2006) 15–19.
[5] M. Batzill, U. Diebold, Prog. Surf. Sci. 79 (2005) 47–154.
[6] L.L. Diaz-Flores, R. Ramirez-Bon, A. Mendoza-Galvan, E. Prokhorov, J. Gonzalez-Hernandez, J. Phys. Chem. Solids 64 (2003) 1037–1042.
[7] D.F. Cox, T.B. Fryberger, S. Semancik, Physical review B 38 (1988) 2072–2083.
[8] T.D. Senguttuvan, L.K. Malhotra, J. Phys Chem Solids 58 (1997) 19–24.
[9] Ç. Kılıç, A. Zunger, Phys. Rev. Lett. 88 (2002) 1–4.
[10] M. Ristic, M. Ivanda, S. Popovic, S. Music, J. Non-Cryst. Solids 303 (2002) 270–280.
[11] P. Veluchamy, M. Tsuji, T. Nishio, T. Aramoto, H. Higuchi, S. Kumazawa, S. Shibutani, J. Nakajima, T. Arita, H. Ohyama, A. Hanafusa, T. Hibino, K. Omura, Sol. Energy Mater. Sol. Cells 67 (2001) 179–185.
[12] M.A. Aegerter, A. Reich, D. Ganz, G. Gasparro, J. Piitz, T. Krajewski, J. Non-Cryst. Solids 218 (1997) 123–128.
[13] P. Siciliano, Sens. Actuators, B 70 (2000) 153–164.
[14] Z. Ji, Z. He, Y.L. Song, K. Liu, Y. Xiang, Thin Solid Films 460 (2004) 324–326.
[15] A.M. Al-Hamdi, M. Sillanpää, J. Dutta, J Rare Earths 33 (2015) 1275–1282.
[16] M. Székely, B. Eid, E. Caillot, M. Herlem, A.E.C. Mathieu, B. Fahys, J. Electroanal. Chem. 391 (1995) 69–75.
[17] L. Prakash, C. Tirupathi, J. Nanosci, Technol. 4 (2018) 478–482.
[18] K. Bouras, G. Schmerber, D. Aureau, H. Rinnert, G. Ferblantier, T. Fix, S. Colis, et al., RSC Adv. 6 (2016) 67157–67165.
[19] Fermin H. Aragon, Ismael Gonzalez, Jos e Ah Coaquira, Pilar Hidalgo, Hermi F. Brito, Jose D. Ardisson, Waldemar Aa Macedo, Paulo C. Morais (2015) The journal of physical chemistry, C 119:8711–8717.
[20] H. Faid, L. Mentar, M.R. Khelladi, A. Azizi, Surf. Engin. 33 (2017) 529.
[21] D. Chu, Y. Masuda, T. Ohji, K. Kato, Chem. Eng. J. 168 (2011) 955.
[22] M. Boubatra, A. Azizi, G. Schmerber, A. Dinia, J. Mater Sci: Mater Electron 22 (2011) 1804.
[23] T. Minami, J. Semicond. Sci. Technol 20 (2005) S35.
[24] M.K. Paria, H.S. Maiti, J. mater Sci 17 (1982) 3275.
[25] M. Gaidi, A. Hajjaji, R. Smirani, B. Bessais, M.A. El Khakani, J. Appl. Phys. 108 (2010) 1–5.
[26] C. Korber, P. Agoston, A. Klein, Sensors Actuators B 139 (2009) 665–672.
[27] D.R. Acosta, W. Estrada, R. Castanedo, A. Maldonado, M.A. Valunzuela, Thin Solid Films 375 (1998) 147–150.
[28] S. Maheshwari, M. Karunakaran, International journal of innovative research in Science, Engineering And Technology 12 (2016) 032395–40056.
[29] G.E. Patil, D.D. Kajale, V.B. Gaikwad, G.H. Jain, Int. Nano Lett 2 (2012) 17.
[30] S. Roguai, A. Djelloul, Solid State Commun. 334–335 (2021), 114362.
[31] S. Chandra, G. George, K. Ravichandran, K. Thirumurugan, Surf. Interfaces 7 (2017) 39–46.
[32] C. Agashe, S.S. Major, J. Phys. D Appl. Phys. 29 (1996) 2988–2991.
[33] C. Agashe, J. Hapkes, G. Schape, M. Berginabi, Sol. Energy Mater. Sol. Cells 93 (2009) 1256–1262.
[34] A. Benhaoua, A. Rahal, B. Benhaoua, M. Jalaci, Superlattice Microst 70 (2014) 61.
[35] S. Palanichamy, J. Raj Mohamed, K. Deva Arun Kumar, P.S. Satheesh Kumar, S. Pandiarajan, L. Amalraj, Optik. 194 (162887) (2019).
[36] A.H. Omran Alkhayatt, S.K. Hussian, Mater. Lett 155 (2015) 109–113.
[37] A. Bouhdjer, A. Attaf, H. Saidi, H. Bendjedidi, Y. Benkhetta, I. Bouhaf, J. Semicond. 36 (2015) 82002.
[38] R. Mariappan, V. Ponnuswamy, M. Ragavendar, D. Krishnamoorthi, C. Sankar, Optik-Int. J. Light Electron. Opt 123 (2012) 1098.
[39] S. Roguai, A. Djelloul, Appl. Phys. A 126 (2020) 122.
[40] O.N. Gavrilenko, E.V. Pashkova, A.G. Belous, Russ. J. Inorg. Chem 52 (2007) 1835.
[41] J. Zhang, L. Gao, J. Solid State Chem. 177 (2004) 1425.
[42] H. Guo, X. Yang, T. Xiao, W. Zhang, L. Lou, J. Mugnier, Appl. Surf. Sci 230 (2004) 215.
[43] Z. Lia, W. Shenb, X. Zhangc, L. Fanga, X. Zua, Colloids and Surfaces A: Physicochem. Eng. Aspects 327 (2008) 17.
[44] G.L. Zou, R. Liu, W.X. Chen, Z.D. Xu, Mater. Res. Bull. 42 (2007) 1153.
[45] S. Roguai, A. Djelloul, C. Nouveau, T. Souier, A.A. Dakhel, M. Bououdina, J. Alloys Compd 599 (2014) 150–158.
[46] A. Hafdallah, F. Ynineb, W. Daranfed, N. Attaf, M.S. Aida, Revue Nature Technologie 6 (2012) 25–27.
[47] E. Burstein, Phys. Rev. 93 (1954) 632–633.
[48] N.F. Habubi, K.A. Mishjil, S.S. Chiad, Indian J Phys 87 (2013) 235–239.
[49] S. Roguai, A. Djelloul, Appl Phys A 125 (2019) 816.
[50] S. Roguai, A. Djelloul, Roles of Cobalt Doping on Structural and Optical of ZnO Thin Films by Ultrasonic Spray… DOI: https://doi.org/10.5772/intechopen.95920.
[51] J.P. Chatelon, C. Terrier, J.A. Roger, Semicond. Sci. Technol. 14 (1999) 642–647.
[52] F. Urbach, The long–wavelength edge of photographic sensitivity and electronic absorption of solids, APS J Phys Rev 92 (1953) 1324–1326.
[53] A.S. Ryzhikov, R.B. Vasiliev, M.N. Rumyantseva, L.I. Ryabova, G.A. Dosovitsky, A. M. Gilmutdinov, V.F. Kozlovsky, A.M. Gaskov, Mater. Sci. Eng., B 96 (2002) 268–274.
[54] S.K. Song, Physical review B 60 (1999) 11137–11148.
[55] L.S. Roman, R. Valaski, C.D. Canestraro, E.C.S. Magalhaes, C. Persson, R. Ahuja, E. F. da Silva Jr, I. Pepe, A. Ferreira da Silva, Appl. Surf. Sci. 252 (2006) 5361–5364.
[56] M. Anitha, K. Saravanakumar, N. Anitha, L. Amalraj, Appl. Surf. Sci. 443 (2018) 55–67.
[57] T.W. Kim, D.U. Lee, J.H. Lee, Y.S. Yoon, Solid State Commun. 115 (2000) 503–507.
[58] Z. Ji, Z. He, Y.L. Song, K. Liu, Z.Z. Ye, J. Cryst. Growth 259 (2003) 282–285.
[59] A. Zevalkink, D.M. Smiadak, J. Blackburn, A.J. Ferguson, M.L. Chabinyc, O. Delaire, J. Wang, K. Kovnir, J. Martin, L.T. Schelhas, T.D. Sparks, S.D. Kang, M. T. Dylla, G.J. Snyder, B.R. Ortiz, E.S. Tobere, Appl. Phys. Rev. 5 (2018), 021303.
[60] T. Tsubota, S. Kobayashi, N. Murakami, T. Ohno, Journal of Electronic Materials. DOI: 10.1007/s11664-014-3227-x.
[61] A. Vora-ud, T. Seetawan, W. Somkhunthot, N. Pimpabute, T. Burinprakhon, Energy Procedia 61 (2014) 2355–2358.
[62] J. Boy, M. Handwerg, R. Ahrling, R. Mitdank, G. Wagner, Z. Galazka, S.F. Fischer, APL Mater. 7 (2019), 022526.
[63] K.J. Godinho, A. Walsh, G.W. Watson, J. Phys. Chem. C 113 (2009) 439.
[64] D.K.S. MacDonald, Thermoelectricity: an introduction to the principles, Wiley, New York, London, 1962.
[65] Z.Q. Li, Y.L. Yin, X.D. Liu, L.Y. Li, H. Liu, Q.G. Song, J. Appl. Phys. 106 (2009), 083701.
[66] C. Bhattacharya, H.C. Lee, A.J. Bard, J. Phys. Chem. C 117 (2013) 9633.
[67] S. Roguai, A. Djelloul, Reaction Kinetics, Mechanisms and Catalysis 132 (2021) 1225–1244.
[68] R. Xie, J. Su, M. Li, L. Guo, Int. J. Photoenergy 2013 (2013) 07.
[69] G. Lente, Deterministic kinetics in chemistry and systems biology, Springer, New York, 2015, pp. 52–58.
[70] M.A. Chakhoum, A. Boukhachem, M. Ghamnia, N. Benameur, N. Mahdhi, K. Raouadi, M. Amlouk, Molecular and Biomolecular Spectroscopy 205 (2018) 649–660.
[71] X. Zhang, Q. Liu, Mater Lett 6 (2008) 2589–2592.
[72] A.J. Zaleska, W. Sobezak, E. Grabowska, J. Hupka, Appl Catal B:Environ. 78 (2008) 92–100.